Journal of Biomedical Optics

SPIEDigitalLibrary.org/jbo

High-resolution three-dimensional imaging of red blood cells parasitized by *Plasmodium falciparum* and *in situ* hemozoin crystals using optical diffraction tomography

Kyoohyun Kim
HyeOk Yoon
Monica Diez-Silva
Ming Dao
Ramachandra R. Dasari
YongKeun Park

SPIE

High-resolution three-dimensional imaging of red blood cells parasitized by *Plasmodium falciparum* and *in situ* hemozoin crystals using optical diffraction tomography

Kyoohyun Kim,[a*] HyeOk Yoon,[a*†] Monica Diez-Silva,[b] Ming Dao,[b] Ramachandra R. Dasari,[c] and YongKeun Park[a]
[a]Korea Advanced Institute of Science and Technology, Department of Physics, Daejeon 305-701, Republic of Korea
[b]Massachusetts Institute of Technology, Department of Material Science and Engineering, Cambridge, Massachusetts 02142
[c]Massachusetts Institute of Technology, George R. Harrison Spectroscopy Laboratory, Cambridge, Massachusetts 02194

Abstract. We present high-resolution optical tomographic images of human red blood cells (RBC) parasitized by malaria-inducing *Plasmodium falciparum* (*Pf*)-RBCs. Three-dimensional (3-D) refractive index (RI) tomograms are reconstructed by recourse to a diffraction algorithm from multiple two-dimensional holograms with various angles of illumination. These 3-D RI tomograms of *Pf*-RBCs show cellular and subcellular structures of host RBCs and invaded parasites in fine detail. Full asexual intraerythrocytic stages of parasite maturation (ring to trophozoite to schizont stages) are then systematically investigated using optical diffraction tomography algorithms. These analyses provide quantitative information on the structural and chemical characteristics of individual host *Pf*-RBCs, parasitophorous vacuole, and cytoplasm. The *in situ* structural evolution and chemical characteristics of subcellular hemozoin crystals are also elucidated. [DOI: 10.1117/1.JBO.19.1.011005]

Keywords: red blood cell; malaria; quantitative phase microscopy; digital holographic microscopy; three-dimensional optical imaging.

Paper 130098SSR received Feb. 23, 2013; revised manuscript received May 6, 2013; accepted for publication May 29, 2013; published online Jun. 25, 2013.

1 Introduction

Human malaria, a mosquito-borne infectious disease linked to two major species of protozoan parasites, *Plasmodium falciparum* and *Plasmodium vivax*, resulted in approximately 660,000 deaths in 2010 from among over 219 million documented episodes, particularly affecting young children in Africa.[1] Parasites, transmitted by mosquitoes, invade and multiply inside the host red blood cells (RBC). During the 48-h intraerythrocytic cycle, the host RBCs undergo significant structural and biochemical modification regulated by complex molecular activities of the parasites. Our understanding of how malaria parasites orchestrate these mechanisms still remains incomplete.

Direct imaging of the three-dimensional (3-D) structures and dynamics of the *P. falciparum* (*Pf*)-RBCs may hold the key to develop a better understanding of the process of malaria infection.[2,3] Soft x-ray tomography provides structural information with extremely high spatial resolution,[4,5] but it requires large-scale synchrotron x-ray facilities, and it does not access the dynamics of live cells. Recent advances in optical microscopy techniques have been employed for the study of structural and physical properties of RBCs altered by malaria parasitization.[6] Fluorescence confocal microscopy, requiring the use of exogenous labeling agents rendering high-contrast molecular information, has also been used to visualize the 3-D shape of *Pf*-RBCs.[7] However, its drawbacks include possible photo-bleaching, photo-toxicity, and interference with normal molecular activities. Recently, refractive index (RI), an intrinsic optical property of materials including biological cells and subcellular components, has been studied to link the structure of RBCs with their physical properties modulated by malarial infection.[8,9]

Measuring the RI offers a means to probe, noninvasively and quantitatively, the structural and chemical information of biological cells[10] including morphology,[11–14] dynamics of the cell membrane,[15–17] dry mass of the cell,[18,19] and concentration of specific molecules in the living cells.[20,21] A series of optical tomographic techniques has been developed to measure the 3-D distributions of RI in biological cells. They include: (1) digital holographic microscopy or quantitative phase microscopy methods to measure multiple transmitted electric field (E-field) with various angles of illumination[22–25] or with sample rotation[26,27] and (2) optical sectioning methods based on low-coherent interference such as optical coherence microscopy[28,29] and optical gating based on interferometric imaging with broadband fields such as spatial light interference tomography.[30,31] Recent studies reported that RI invoked multiple wavelength digital holograms obtained by tomographic holography, which circumvents the need for mechanical scanning,[32,33] as well as a noninterferometric imaging technique which quantified cellular RI and dry mass density using a standard trans-illumination optical microscope.[34]

Among these various techniques and applications, RBCs have been studied with 3-D RI tomography with unique advantages.[8,9] RBCs have a relatively simple two-dimensional (2-D) cytoskeletal structure without a nucleus. Therefore, 3-D RI measurement can directly provide structural information about the cell membrane. RBC cytoplasm mainly consists of hemoglobin (Hb) protein, and the RI of RBC cytoplasm can

*Contributed equally to this work.
†Present address: Stanford University, Department of Applied Physics, Stanford, California 94305.

Address all correspondence to: YongKeun Park, Korea Advanced Institute of Science and Technology, Department of Physics, 291 Daehak-Ro Yusung-Gu, Daejeon 305-701, Republic of Korea. Tel: (82) 42-350-2514; Fax: (82) 42-350-7160; E-mail: yk.park@kaist.ac.kr

0091-3286/2014/$25.00

be directly translated into chemical information about Hb inside the cell.[8] Furthermore, the structural and chemical information probed by measuring the RI could be strongly correlated with RBC pathophysiology, including malaria infection[6,8,9] and sickle cell disease,[35–37] and with different biochemical conditions introduced by different levels of osmotic pressure[17] and ATP metabolism.[16,38,39]

Recently, 3-D RI tomography has been employed for noninvasively measuring the structural and biochemical information of *Pf*-RBCs,[8] and studying the mechanistic processes associated with parasite egress following the intraerythrocytic cycle.[9] Tomographic phase microscopy has been utilized to measure the multiple E-fields measurements with various illumination angles from which the 3-D RI tomograms of the *Pf*-RBCs are reconstructed using a projection algorithm.[8,40] Reconstruction using the projection algorithm, assuming no diffraction of light in the sample, is computationally simple but does not generally provide a precise 3-D RI distribution, especially for a sample with inhomogeneous distribution of RI values. The parasitization of RBCs results in the formation of several optically inhomogeneous structures including digestive food vacuoles (a major digestive organelle of the malaria parasite), hemozoin (a disposal product formed from the digestion of Hb by parasites), and knobs (nanometer-scale protuberances in the *Pf*-RBC membrane conferring adherence to vascular endothelia).[41] All these structures exhibit highly inhomogeneous RI distribution, and thus can significantly cause refraction, reflection, and diffraction of light. Consequently, the 3-D RI tomograms of the *Pf*-RBCs extracted solely from optical projection have limitations in imaging quality and resolution.

Here, we report high-resolution 3-D optical tomograms of *Pf*-RBCs constructed using a 3-D optical diffraction tomography algorithm. We show that compared with earlier reports based on the projection algorithm, the present 3-D RI tomograms extracted with a diffraction algorithm provide highly detailed structural information as well as more precise RI values. We compare the 3-D RI tomograms of the *Pf*-RBC with the entire 48-h intraerythrocytic cycle using both diffraction- and projection-based reconstruction algorithms. We report quantitative estimates of host *Pf*-RBC volume, parasitophorous vacuole volume, and cytoplasmic volume over the entire intraerythrocytic maturation stages of the parasite. We also investigate the structural and chemical characteristics of *in situ* hemozoin development inside the *Pf*-RBCs.

2 Theory

Reconstruction of a 3-D tomogram from the multiple 2-D E-fields with various illumination angles is performed by two methods: the projection and the diffraction algorithms. Since the diffraction algorithm generally considers the effect of diffraction—the interaction between light and matter—it addresses the challenges present in the projection algorithm such as limited spatial resolution and low image quality.[23,24,42,43] Figure 1 shows a schematic diagram explaining the reconstruction processes of the two algorithms.

In the projection algorithm, diffraction of light in a sample is assumed to be negligible; light is assumed to propagate along straight lines with unchanged spatial frequency vectors, k. The projection algorithm can be implemented by the filtered backpropagation method.[40,44] A single 2-D E-field image from a specific illumination angle corresponds to an inclined plane, corresponding to the incident angle in Fourier space (Fourier slice theorem), and the center of the inclined plane is located at the origin of the Fourier space [Fig. 1(b)]. Consequently, in the projection algorithm, all the measured 2-D E-fields with various illumination angles will map a bow-tie-shaped object function distribution in Fourier space. Inverse 3-D Fourier transformation of the objective function then provides a 3-D optical

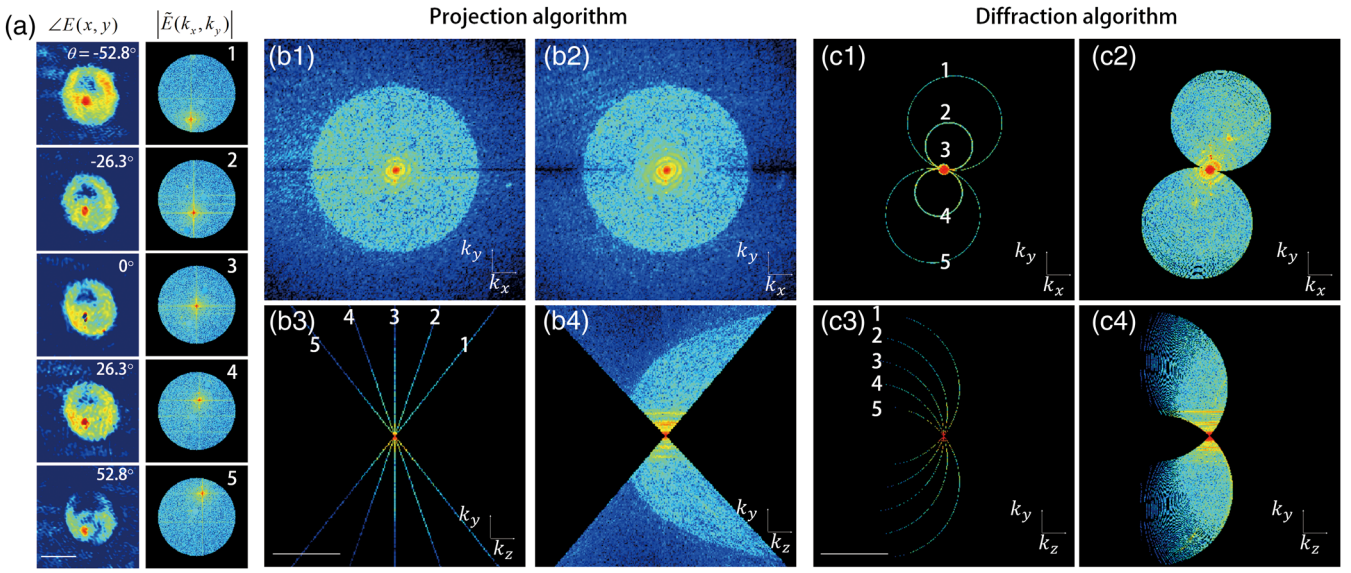

Fig. 1 Comparison of various three-dimensional (3-D) reconstruction algorithms. (a) Quantitative phase images of a *Plasmodium falciparum*-red blood cells (*Pf*-RBC) in trophozoite stage measured at various illumination angles (left) and corresponding spectrum in Fourier space (right). (b–c) Object functions in Fourier space reconstructed by (b) the projection algorithm and (c) the diffraction algorithm. (b1) Amplitude distributions of the object function reconstructed by the projection algorithm in the $k_x - k_y$ plane with five representative illuminations angles and (b2) with the full illumination angles. The corresponding amplitude distributions in the $k_z - k_y$ plane are shown in (b3) and (b4), respectively. (c1) Amplitude distributions of the object function reconstructed by the diffraction algorithm in the $k_x - k_y$ plane with five representative illuminations angles and (c2) with the full illumination angles. The corresponding amplitude distributions in the $k_z - k_y$ plane are shown in (c3) and (c4), respectively.

tomogram of the sample. The mapping process in the projection algorithm can be easily performed by applying inverse Radon transformation.[45] A set of 2-D E-field images with various illumination angles, a so-called sinogram, can be converted into a 3-D tomogram. Full details of the projection algorithm can be found elsewhere.[40,44]

In contrast, the diffraction tomography algorithm, originally established by Wolf,[42] takes diffraction of light into account. Recently, the diffraction algorithm has been successfully employed for retrieving high-resolution 3-D structures of weakly scattering samples.[23,42,43] The diffraction algorithm can be implemented with either the Born[46] or Rytov[47] approximations. The Born and the Rytov approximations both take the incident field as the driving field at each point of the scatterer. While both the Born and Rytov approximations consider the scattered E-field due to the presence of a sample, the Born approximation is valid for a weak scattering field from a relatively small sample. The Born approximation can be applied for a large object, provided the RI contrast is low. However, the Rytov approximation is valid as long as the phase gradient in the sample is small and is independent of the sample size. In this study, we used the Rytov approximation. Rytov approximation works independently of the size of an object, whereas Born approximation depends on the size of an object.[42] In the diffraction algorithm with the Rytov approximation, the spatial frequencies of the scattered E-fields from one illumination angle cover a 2-D hemispheric surface, the so-called Ewald sphere [Fig. 1(c)]. The peak intensity of the surface, implying the lowest spatial frequency from an unscattered field, matches the origin at the Fourier space, and the range of the Ewald surface is limited by the numerical aperture (NA) of the optical imaging system.[23,48] Thus, the scattered E-fields from all the possible illumination angles form a butterfly-shaped object transfer function. Inverse 3-D Fourier transformation of the object function is mapped via the diffraction algorithm, and then provides a 3-D tomogram of the sample. The details on the diffraction algorithm can be found elsewhere.[43,48–50]

3 Materials and Methods

3.1 *Experimental Setup*

The detailed experimental setup for measuring E-fields with various illumination angles has been described in previous works.[40,43] Briefly, complex E-fields images are recorded by Mach–Zehnder interferometry. A laser beam from a He-Ne laser ($\lambda = 633$ nm, 10 mW, unpolarized light, Throlabs, Newton, New Jersey) is split into two arms. One arm can be tilted by a galvano mirror (GVS012, Throlabs) and illuminates samples with various angles of illuminations. The diffracted beam from the sample is collected by a high NA objective lens (UPLSAPO, 100×, NA = 1.4, Olympus Inc., Center Valley, Pennsylvania) and a tube lens ($f = 200$ mm). Then, the beam is further magnified by an additional $4f$ lens system so that the total lateral magnification is 210×. The diffracted beam from the sample interferes with a reference beam and generates spatially modulated interferograms, which are recorded by a high-speed CMOS camera (1024 PCI, Photron USA Inc., San Diego, California). Typically, 600 2-D holograms of the sample, illuminated by plane waves with illumination angles (−70 deg to 70 deg at the sample plane), are recorded for the reconstruction of one tomogram.

The complex amplitude (amplitude and phase) of the E-fields images is then extracted from the measured interferograms using the field retrieval algorithm (see Ref. 51 for field retrieval algorithms). Diffraction tomograms are mapped in 3-D Fourier space using multiple 2-D E-field images, and then reconstructed by using a 3-D inverse Fourier transformation (refer to Supporting Materials for the MatLab code used for the reconstruction). The projection tomograms are reconstructed from the sequential E-fields maps with various illumination angles via inverse Radon transformation.

Due to the limited angle of acceptance of the imaging system, or NA, there is missing information in the 3-D Fourier spectrum for both the projection and diffraction algorithms [Fig. 1(b) and 1(c)]. Even with the high NA objective lens, only a fraction of the scattered light from the sample can be utilized for optical imaging. To fill this information due to the limited NA, the iterative constraint algorithm[43,52] was executed to the tomograms reconstructed from both the projection and diffraction algorithms. The following constraints were invoked in the interactive algorithm in the present study:

1. The surrounding medium has a known fixed RI.
2. The RI of *Pf*-RBCs cannot be smaller than that of the surrounding medium.

Applying the iterative algorithm fills the information corresponding to the missing angles with appropriate values. All data analysis was performed using custom-made scripts in MatLab (MathWorks Inc., Natick, MA) on a desktop computer (Inter Core i5-2600 CPU, 3.4 GHz, 8 GB RAM). The MatLab codes used for optical tomographic reconstruction based on diffraction algorithm are included in Supporting Information S1. The computation times for reconstructing a 3-D RI tomogram (size of $380 \times 380 \times 380$ matrix) are typically 100 and 200 s for the projection and diffraction algorithms, respectively. The iterative algorithm takes approximately 100 iterations for the diffraction algorithm, corresponding to ∼3000-s computation time, whereas the projection algorithm takes approximately 15 iterations (3000-s computation time.)

3.2 *Sample Preparation*

P. falciparum (3D7) parasites were maintained in leukocyte-free human O+ erythrocytes (Research Blood Components, Boston, Massachusetts), stored at 4°C for no longer than two weeks under an atmosphere of 3% O_2, 5% CO_2, and 92% N_2 in RPMI 1640 medium (Gibco Life Technologies, Carlsbad, California) supplemented with 25 mM HEPES (Sigma-Aldrich, St. Louis, Missouri), 200 mM hypoxanthine (Sigma-Aldrich), 0.209% $NaHCO_3$ (Sigma-Aldrich) and 0.25% albumax I (Gibco Life Technologies). Cultures were synchronized successively by a concentration of mature schizonts using plasmagel flotation[53] and sorbitol lysis 2 h after merozoite invasion to remove residual schizonts.[54] The sample preparation procedures and the methods were approved by the Institutional Review Board.

Upon measurement, *Pf*-RBC samples were first diluted in phosphate-buffered saline (PBS) solution to approximately 10^6 RBC/ml. Ten microliters of the diluted samples were sandwiched between two cover glasses. Measurements were performed at 14 to 20 h (ring stage), 20 to 36 h (trophozoite stage), and 36 to 48 h (schizont stage) following merozoite invasion.

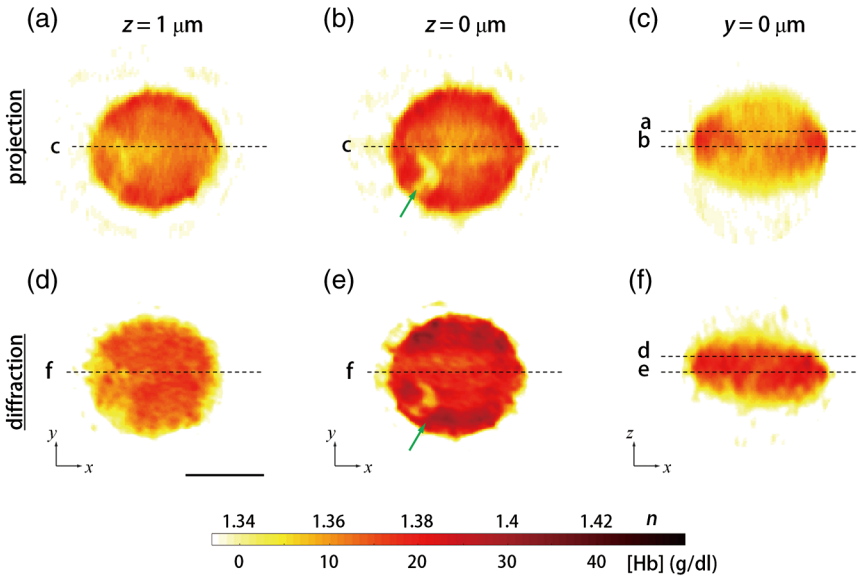

Fig. 2 Refractive index (RI) maps of a *Pf*-RBC at the ring stage. (a–c) *x*–y cross-sectional slices of RI distribution mapped with the projection algorithm at (a) 1 μm above the focal plane, (b) the focal plane, and (c) the *x*–z plane at the center. (d–f) Slices of RI distribution mapped with the diffraction algorithm. Green arrow indicates malaria parasite. Each dashed line stands for corresponding slices. Scale bar indicates 5 μm.

4 Results

4.1 *3-D RI Tomograms of Pf-RBCs Based on Diffraction Algorithm*

The 3-D RI tomograms of 26 *Pf*-RBCs were measured throughout the full intraerythrocytic states (8, 13, and 5 cells for ring, trophozoite, and schizont stages, respectively) For each individual *Pf*-RBC, 600 E-field holograms with various illumination angles (−70 deg to +70 deg) were measured from which both projection and diffraction tomograms were reconstructed by respective algorithms. The projection and diffraction tomograms from the representative *Pf*-RBCs at each intraerythrocytic state are shown in Figs. 2–4.

Each figure shows cross-sectional maps of the 3-D RI tomograms reconstructed by either the projection (upper row) or the diffraction algorithm (lower row) at various planes: 1 μm above the focal plane (left column), the focal plane (center column) along the axial direction, and $x-z$ plane at the center of the sample (right column). Since the cytoplasm of RBCs consists mainly of Hb, cytoplasmic Hb concentration for individual RBCs can be calculated from the measured RI.[8] The RI of Hb solution is directly related to the concentration of Hb.[55,56] The real part of the RI n is proportional to the cytoplasmic Hb concentration C as

$$n = n_0 + \alpha C, \tag{1}$$

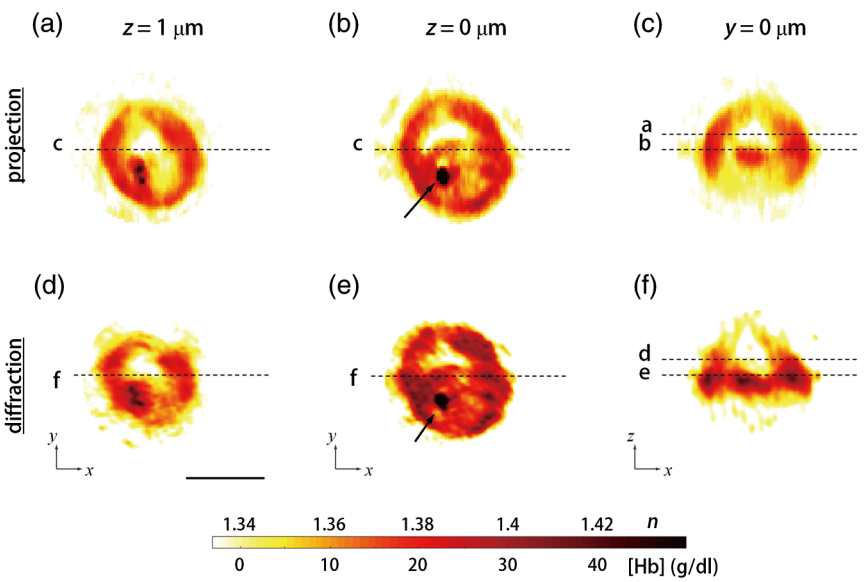

Fig. 3 RI maps of a *Pf*-RBC at the trophozoite stage. (a–c) *x*–y cross-sectional slices of RI distribution mapped with the projection algorithm at (a) 1 μm above the focal plane, (b) the focal plane, and (c) the *x*–z plane at the center. (d–f) Slices of RI distribution mapped with the diffraction algorithm. Black arrow indicates hemozoin. Scale bar indicates 5 μm.

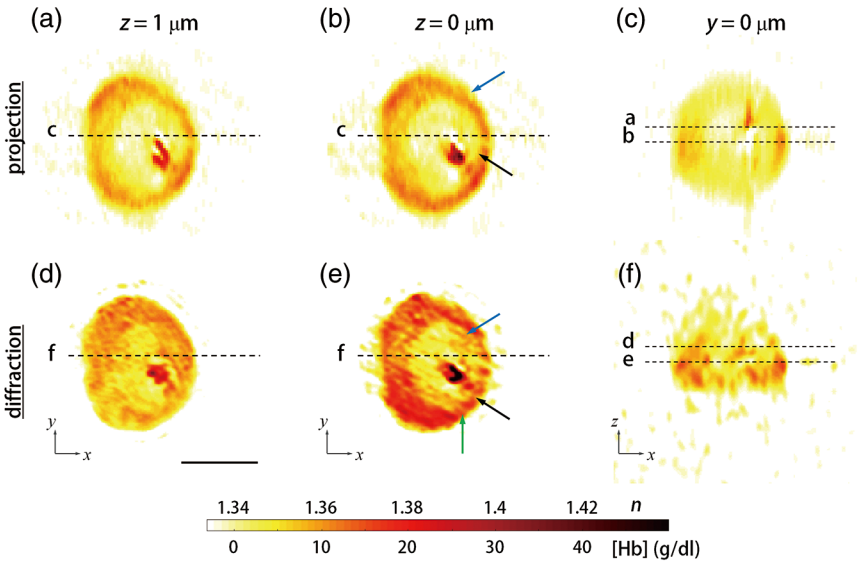

Fig. 4 RI maps of a *Pf*-RBC at the schizont stage. (a–c) $x-y$ cross-sectional slices of RI distribution mapped with the projection algorithm at (a) 1 μm above the focal plane, (b) the focal plane, and (c) the $x-z$ plane at the center. (d–f) Slices of RI distribution mapped with the diffraction algorithm. Black arrow: hemozoin and blue arrow: plasmodium vacuoles. Scale bar indicates 5 μm.

where n_0 is the RI of the surrounding medium ($n_0 = 1.334$ at $\lambda = 633$ nm) and α is the specific refractive increment ($\alpha = 0.144$ ml/g for both oxygenated and deoxygenated hemoglobin at $\lambda = 633$ nm).[8,20,55,56]

The 3-D RI tomograms of *Pf*-RBCs at the ring stage clearly show a ring-shaped internal structure inside the host *Pf*-RBC, which corresponds to an invaded parasite having an RI smaller than that of the cytoplasmic area (green arrows, Fig. 2). At the focal plane, both diffraction and projection algorithms provide comparable structures. However, above and below the focal plane, the tomogram reconstructed with the projection algorithm shows blurry cell boundaries that are extended in the axial direction, whereas the diffraction tomogram shows more distinct cell boundaries. More importantly, cross-section images reconstructed by the projection algorithm provide incorrectly elongated shapes in the z-direction [Fig. 2(c)]. This is due to the omission of light diffraction in the projection algorithm; light diffraction at the RBC boundaries can be only taken into account in the diffraction reconstruction algorithm. Considering the complex shape of the RBC membrane and the RI difference between the surrounding medium and the cell cytoplasm (~0.04 to 0.06, depending on the Hb concentration), the plane wave impinging into the RBC may exhibit both refraction and reflection, thus resulting in significant diffraction of the transmitted beam. The RI tomogram of *Pf*-RBCs not only shows morphological information regarding the cell and its subcellular structures, but also enables us to obtain the biochemical information of the *Pf*-RBCs; the cytoplasmic RI can be directly translated into quantitative information about Hb concentration and total Hb contents.[8]

The effect of light diffraction becomes more significant in the later stages. The 3-D RI tomograms of the *Pf*-RBCs at the trophozoite stage show more difference between the reconstructions with the projection and diffraction algorithms (Fig. 3). Distinct differences can be observed, especially for the extremely high RI values in the cytoplasm, indicating the hemozoin structure (black arrows, Fig. 3). As they grow inside the host RBCs, the parasites metabolize Hb and produce hemozoin—an insoluble crystallized form of free heme, the nonprotein component of Hb, having a high RI ($n \geq 1.42$). At the trophozoite stage, the overall shape of the *Pf*-RBCs membrane becomes more complex, and malaria byproducts are newly generated as substructures with significantly high RI values and with a high spatial gradient.

The 3-D RI tomograms of the *Pf*-RBCs in the schizont stage show significantly decreased RI in the cytoplasm (Fig. 4), which is consistent with a previous report.[8] The 3-D RI tomograms reconstructed with the diffraction algorithm clearly show plasmodium vacuoles generated by the parasites (blue arrows). By contrast, the tomogram reconstructed with the projection algorithm does not provide high-resolution details on these subcellular structures.

The structural and biochemical alterations resulting from the parasitization of the host *Pf*-RBC inevitably cause significant light diffraction from the sample. Severe structural alterations in the schizont stage *Pf*-RBCs can result in more light diffracted in the *Pf*-RBCs. In addition, significant reorganization of Hb proteins can also contribute more light diffraction; most of the cytoplasmic Hb is digested by the parasites, and then converted into hemozoin with high RI values. The use of the diffraction reconstruction algorithm could provide more precise 3-D RI tomograms. On the other hand, the projection algorithm does not support the appearance of light diffraction from the sample. As shown in Figs. 2–4, the reconstruction with the diffraction algorithm provides more precise 3-D RI tomograms of the *Pf*-RBCs with finer details. For comparison purposes, the projection and diffraction tomograms from healthy RBCs are also shown in Fig. 5. Similar to the *Pf*-RBCs, the tomograms of the healthy RBCs reconstructed by the diffraction algorithm show less distortion in their shapes than the ones obtained with the projection algorithm.

Based on the tomograms of the *Pf*-RBCs reconstructed by the diffraction algorithm, 3-D isosurfaces are rendered, as shown in Fig. 6 (see also Multimedia movies). The cell membranes of the *Pf*-RBCs are represented for the outer surface having the cytoplasmic RI; subcellular structures such as hemozoin, plasmodium vacuoles, and malaria parasites are also visualized as surfaces by connecting the specific refractive indices. The

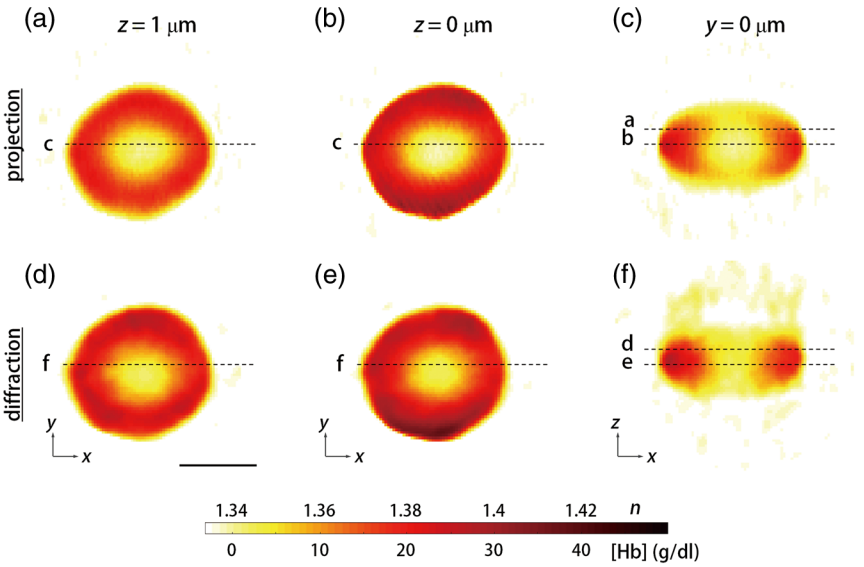

Fig. 5 RI maps of a healthy RBC. (a–c) *x*–y cross-sectional slices of RI distribution mapped with the projection algorithm at (a) 1 μm above the focal plane, (b) the focal plane, and (c) the *x*–z plane at the center. (d–f) Slices of RI distribution mapped with the diffraction algorithm. Scale bar indicates 5 μm.

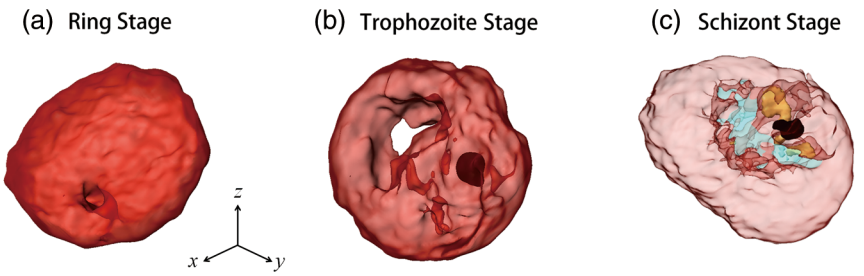

Fig. 6 Rendering of the RI isosurfaces of *Pf*-RBCs at (a) the ring (Video 1, QuickTime, 4 MB) [URL: http://dx.doi.org/10.1117/1.JBO.19.1.011005.1], (b) the trophozoite (Video 2, QuickTime, 6 MB) [URL: http://dx.doi.org/10.1117/1.JBO.19.1.011005.2], and (c) the schizont stage (Video 3, QuickTime, 6 MB) [URL: http://dx.doi.org/10.1117/1.JBO.19.1.011005.3]. The length of arrows corresponds to 1 μm.

3-D RI tomogram reconstructed with the diffraction algorithm shows the shapes and locations of the parasites as well as other associated structures in high detail. Rendering was performed by commercial software (Amira 5, Visage Imaging Inc., San Diego, California). The structures of *Pf*-RBCs depicted in 3-D RI tomograms are comparable with those obtained with high-resolution scanning electron microscopy.[4,5]

4.2 *Cytoplasmic Volumes Calculated by Different Reconstruction Algorithms*

Compared with the projection tomogram, the diffraction tomograms of 3-D RI of the *Pf*-RBCs not only provide high-resolution structural details, but also enable the determination of biochemical information about the Hb content with higher precision. To quantitatively compare the effects of using the different reconstruction algorithms with respect to chemical information, we calculated the cytoplasmic volume and mean cellular Hb concentration (MCHC) values of the *Pf*-RBCs with both the projection and diffraction tomograms. The cytoplasmic volume and MCHC values are important parameters for hemodiagnosis.

The MCHC values of each *Pf*-RBC calculated from the reconstructed RI tomograms do not show statistical differences between the projection and diffraction algorithms. This can be readily understood by the fact that, in principle, both algorithms should give comparable RI values of an object at the focal plane since the effect of diffraction of the propagated beam is minimized at the focal plane. The cytoplasmic volumes, however, show significant differences between the projection and diffraction algorithms (Fig. 7). Overall, the mean cytoplasmic volumes calculated from the projection algorithm are 33% higher than those calculated from the diffraction algorithm. In addition, the values retrieved with the diffraction algorithm showed narrower distribution among the *Pf*-RBCs. The difference in the values of cytoplasmic volume calculated by different reconstruction algorithm can be explained by the fact that, in the projection algorithm, the diffraction of light is not considered except at the focal plane, and thus, the reconstructed shapes of the RBC membrane can be severely distorted.

4.3 *Volumes of Pf-RBC, Cytoplasm, and Parasitophorous Vacuole at Individual Cell Level*

To address the structural alterations of *Pf*-RBC during intraerythrocytic cycle, we calculate the volumes of host *Pf*-RBC, RBC cytoplasm, and parasite at individual cell levels, from the measured 3-D RI tomograms reconstructed by diffraction algorithm based on the Rytov approximation (Fig. 8). Since the 3-D RI tomograms provide quantitative information about

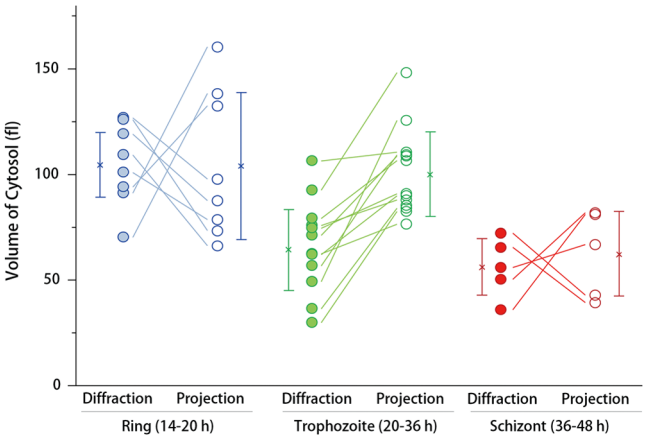

Fig. 7 Cytoplasmic volumes calculated by different reconstruction algorithms. Circular symbols represent individual *Pf*-RBCs. Dashed lines connect the values of the same cell calculated with the different algorithms. The cross symbols represent the median values, and the vertical lines indicate standard deviations.

morphologies of individual *Pf*-RBCs, the volumes of *Pf*-RBC, cytoplasm, and parasite are measured at the individual cell level.

The whole host *Pf*-RBC volumes were calculated by integrating volumes inside individual *Pf*-RBCs. The cytoplasmic volumes were obtained by integrating volumes in which RI values are within a specific range ($1.34 \leq n \leq 1.42$) in order to select cytoplasm-containing Hb solution, and the space corresponding to parasitophorous vacuoles (with hemozoin inside) was excluded. Then, the volumes for parasitophorous vacuole were calculated by subtracting the whole host *Pf*-RBC volumes from cytoplasmic volumes.

Despite the large cell-to-cell variations in the measurements, it is clear from the results that the total volumes of *Pf*-RBCs increase as the intraerythrocytic stage progresses. The mean values of the total *Pf*-RBCs volumes are 117.6 ± 17.7 fl (ring), 106.9 ± 17.4 fl (trophozoite), and 132.7 ± 29.7 fl (schizont) [Fig. 8(a)]. This increase of total *Pf*-RBC volumes is caused by the enlargement of parasite volumes even though cytoplasmic volume, corresponding to host cell water volume, decreases. Cytoplasmic volumes (host cell water volume) are measured to be 105.0 ± 18.3 fl (ring), 65.3 ± 20.7 fl (trophozoite), and 56.0 ± 14.0 fl (schizont) [Fig. 7(b)]. The mean values of the parasitophorous vacuole volumes are 12.7 ± 8.3 fl (ring), 40.3 ± 16.0 fl (trophozoite), and 75.90 ± 30.3 fl (schizont) [Fig. 7(c)].

Our results are in good agreement with the previous measurements obtained with independent techniques (Fig. 8). Zanner et al. reported cytoplasmic volumes and *Pf*-RBC volumes measuring diffusive water permeability using stopped-flow spectroscopy.[57] Elliott et al. measured the transport of lactate and pyruvate in *Pf*-RBC,[58] and employed serial thin-section electron microscopy and 3-D reconstruction[59] in order to measure whole *Pf*-RBC volumes as well as parasite values. Recently, Esposito et al. measured total RBC volumes using confocal microscopy.[60] More recently, Hanssen et al. determined parasitophorous volumes of *Pf*-RBCs using cryo x-ray tomography.[4] Although the previous techniques have measured the values at different time scales with different sensitivities, their values of the total *Pf*-RBCs volumes are 75 to 100 fl (ring), 130 to 150 fl (trophozoite), and 50 to 160 fl (schizont). Previously measured cytoplasmic volumes are 75 to 100 fl (ring), 25 to 100 fl (trophozoite), and 10 to 80 fl (schizont) [Fig. 8(b)]. The previously measured values of the parasitophorous vacuole volumes are 5 to 20 fl (ring), 5 to 50 fl (trophozoite), and 30 to 100 fl (schizont). In addition, our measured values are also consistent with mathematical model simulations.[61]

4.4 *3-D RI Tomograms of In Situ Formation of Hemozoin Crystals*

To further show the capability of 3-D optical tomograms with the diffraction reconstruction algorithm, we perform *in situ* 3-D imaging and structural analysis of the residual bodies containing subcellular hemozoin in *Pf*-RBCs. Hemozoin is a disposal product formed by the malaria parasites as a result of the metabolization of Hb. It accumulates as cytoplasmic crystals in the food vacuole of developing parasites. As *Pf*-RBCs mature from ring stage to trophozoite stage, hemozoins become detectable as brown birefringent crystals via light microscopy[62]. No hemozoin is observed at the ring stage.

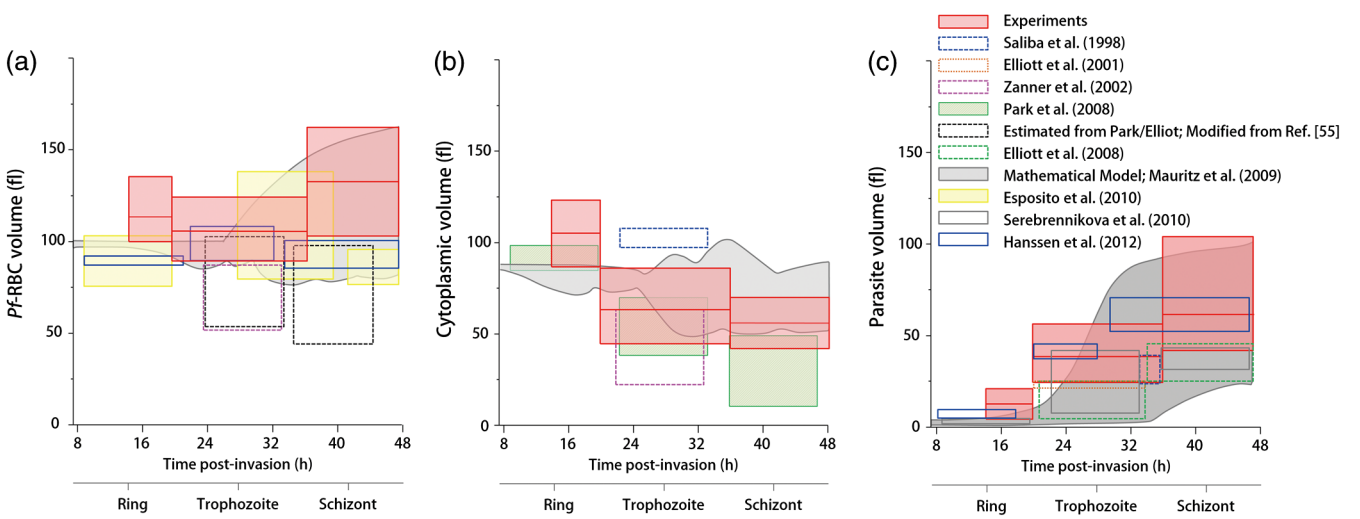

Fig. 8 Measured values of (a) *Pf*-RBC volume, (b) cytoplasmic volume, and (c) parasite volume over intraerythrocytic cycle. Measured values from previous reports were also shown for comparison purpose.

The shape and size of hemozoin provide metabolic information of individual *Pf*-RBCs.[63] Different structural characteristics of hemozoin crystals have been observed for Plasmodium species.[64] From the measured 3-D optical diffraction tomograms of the *Pf*-RBCs, we analyzed hemozoin structures and their optical properties in 16 *Pf*-RBCs (12 trophozoites and 4 schizonts). By selecting positions having RI values higher than a threshold value ($n \geq 1.42$), we retrieved the 3-D volumes of RI corresponding to the residual bodies containing hemozoin in the *Pf*-RBCs [Fig. 9(a)]. In order to investigate the structural characteristics of the hemozoin crystals quantitatively, we calculated the volume and surface area of hemozoin from the *Pf*-RBCs. The measured values for the volume and surface area are 1.08 ± 0.48 fl and 7.25 ± 3.56 μm^2, respectively, for trophozoite stage, and 0.68 ± 0.27 fl and 4.47 ± 1.29 μm^2, respectively, for schizont stage. These values are consistent with previous studies using independent experimental methods. Gligorijevic et al. used spinning disk confocal microscopy and measured the volumes of hemozoin crystals in the range 0.2 to 0.7 fl.[63] Hanssen et al. employed x-ray microscopy and measured the volumes of hemozoin crystals during gametogenesis in the range of 0.6 to 0.8 fl.[4] Although the magnitudes of the measured values for the volume and surface area are in agreement with the previous reports, we note that the decrease in the measured values from trophozoite to schizont stage is not consistent with previous works. This can be partly attributed to the limited number of samples ($n = 12$ and 4 for the number of cells in trophozoite and schizont stage, respectively). Moreover, the sphericity ψ of hemozoin was found to be 0.79 ± 0.11 (trophozoite) and 0.83 ± 0.09 (schizont), which was calculated from the volume and surface area as $\psi = \pi^{1/3}(6V_p)^{2/3}/A_p$.

In addition, 3-D RI tomogram reconstructed with the diffraction algorithm provides complex RI values $n^* = n' + in''$; the real part of RI is a conventional value for RI n that relates the speed of light in the material, whereas the imaginary part of RI corresponds to the absorption coefficient. Absorption coefficient κ, which describes how much a material absorbs light so that illuminated light intensity I_0 is attenuated to I after passing a material with a thickness l, $I = I_0 \exp(-\kappa l)$. κ and n'' are related by Beer–Lambert law as $\kappa = 4\pi n''/\lambda$. The absorption coefficients of the hemozoins are calculated from the imaginary part of RI: n'' of *in situ* hemozoin was found to be 0.048 ± 0.005 (trophozoite) and 0.045 ± 0.008 (schizont), while the rest of *Pf*-RBCs are nearly transparent at the wavelength used ($\lambda = 633$ nm). The measured κ is comparable with the previous report ($n'' = 0.052$; estimated from Ref. 65 with the size of hemozoin is ~0.6 μm) where an UV-VIS absorption spectrometer was used.

The concentration of hemozoin c is calculated from the measured κ based on Beer–Lambert law:

$$c = \kappa/[\epsilon \ln(10)], \tag{2}$$

where ϵ is the molar extinction coefficient (molar absorptivity) of hemozoin which is estimated as 5×10^4 cm^{-1} M^{-1} at 633 nm from Refs. 65 and 66. The hemozoin concentrations were calculated as 40.47 ± 3.85 and 38.09 ± 6.96 g/dl for trophozoite and schizont stages, respectively. Then, by multiplying the molecular weight of hemozoin (4915.9 g/mol), the hemozoin contents of *Pf*-RBCs are retrieved as 0.52 ± 0.33 and 0.26 ± 0.12 pg for trophozoite and schizont stages, respectively. Considering the limited number of samples, especially for the schizont stage, these assured values are also in agreement with previous studies that used UV-VIS absorption spectroscopy (0.72 to 0.76 pg for trophozoite and 0.76 to 0.84 pg for schizont stages).[67] We would like to emphasize that the chemical and structural information of hemozoin were directly measured at the individual intact *Pf*-RBCs for the first time.

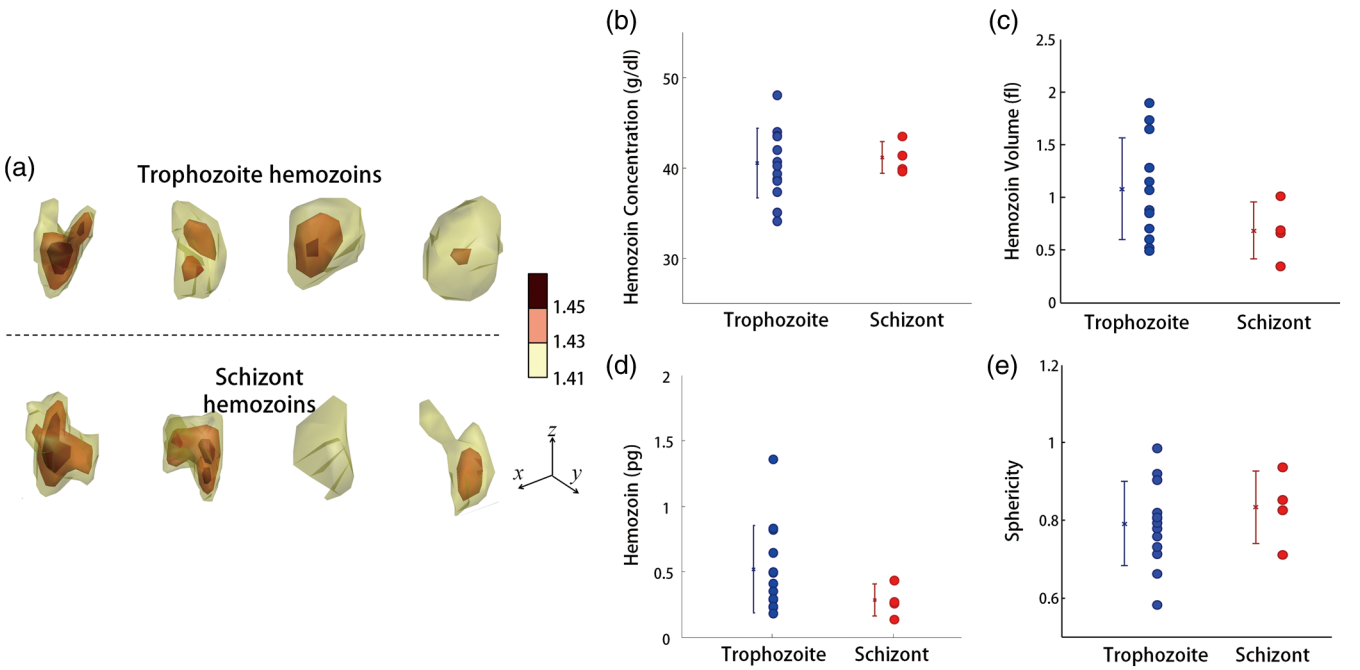

Fig. 9 Characterizations of *in situ* hemozoins. (a) 3-D renderings of representative hemozoins inside *Pf*-RBCs. The length of arrows corresponds to 1 μm. Three isosurfaces with representative RI values are rendered according to the color bar. No hemozoin was observed during the ring stage. (b) Hb concentration in hemozoin. (c) Hemozoin volume. (d) Hemozoin contents. (e) Sphericity of the hemozoin. The cross symbols represent the median values, and the vertical lines indicate standard deviations.

5 Conclusion

In this work, we present high-resolution 3-D optical RI tomograms of *Pf*-RBCs employing the diffraction algorithm for tomogram reconstruction. The structural information about individual *Pf*-RBCs as well as parasitophorous vacuole and cytoplasm of the host *Pf*-RBCs was quantitatively measured. Furthermore, the *in situ* structural and chemical information of hemozoin inside *Pf*-RBCs was also investigated using the optical diffraction tomography. The multiple 2-D E-field images of individual RBCs were measured with various angles of illumination using quantitative phase microscopy from which 3-D tomograms were reconstructed via the diffraction algorithm with Rytov approximation. The RI tomograms of *Pf*-RBCs during the full intraerythrocytic cycle were presented with the diffraction algorithm. The 3-D RI tomograms of the same samples reconstructed by the projection algorithm were also presented and systematically compared. Our results show that the light diffraction effect is significant in *Pf*-RBCs; thus, the RI tomograms obtained with the diffraction algorithm were more precise than those obtained with the projection algorithm. Three-dimensional high-resolution imaging holds a key to revealing the mechanisms behind malaria pathophysiology, and is now accessible to direct experimental study without using exogenous labeling agents. Dynamic measurements of the RI tomograms of *Pf*-RBCs provide further opportunities for the determination of the dynamic properties of *Pf*-RBCs[68] in order to better understand *in vivo* circulation through microcapillaries and spleen sinusoids.

Although the particular focus of this paper is to demonstrate the reconstruction of 3-D RI tomograms of *Pf*-RBCs based on diffraction algorithm, the present approach is sufficiently broad and general and will directly find use in multiple studies. For example, the processes of invasion and egress of this particular parasite and the RBCs invaded with other species of protozoan parasites, such as *P. vivax* or *Plasmodium ovale*, can be investigated with the current approach. Furthermore, the other RBC-related diseases associated with significant morphological alteration including sickle cell diseases are now accessible to direct experimental study using optical tomography.

Appendix: MatLab Code for Optical Diffraction Tomography Algorithm

```
% Optical diffraction tomography reconstruction algorithm
% Programmed by Kyoohyun Kim (Biomedical Optics Lab, KAIST) 2012-8-9
% for further information, please refer to http://bmokaist.wordpress.com.

    % A raw-data file must contain following variables:
    % 1. EField(frame, x, x) is a 3-D complex amplitude (amplitude and phase)
    % matrix for multiple 2-D electric-field images
    % 2. u0_x(frame): x spatial frequency for illumination angle: [pixel]
    % 3. u0_y(frame): y spatial frequency for illumination angle: [pixel]

%% initialization
clear all
n_m=1.334;                          % refractive index of medium, PBS=1.334 @ 633 nm
lambda=0.633;                       % wavelength of the laser [μm]
ZeroPadding_Real=1024;              % # of pixels at image plane (2-D) after zero-padding
ZeroPadding_Fourier3D=600;          % # of pixels at Fourier plane (3-D) after zero-padding
PixSize_CCD=16;                     % pixel size at the CCD plane [μm]
Mag_total=210;                      % total magnification
PixSize_Sample=PixSize_CCD/210;     % pixel size at the sample plane [μm]

%% File Import
load('Field_Trophozoite_04.mat');
[thetaSize xSize ySize]=size(EField);   %ex) xSize=380, ySize=380, thetaSize=600;

%% fitting Incident illumination angles
Frame_range=1:thetaSize;
Frame_normal=300;                   % frame # for normal incident angle
p1=polyfit (Frame_range, u0_x (Frame_range), 1);
p2=polyfit (Frame_range, u0_y (Frame_range), 1);
u0_x=p1(2)+p1(1)*Frame_range;
u0_y=p2(2)+p2(1)*Frame_range;
u0_x=(u0_x - u0_x(Frame_normal))*ZeroPadding_Real/xSize;   %considering zero-padding
u0_y=(u0_y - u0_y(Frame_normal))*ZeroPadding_Real/ySize;

%% Set parameters
k0=2*pi/lambda;                     % k vector (angular spatial frequency) of incident beam
```

```
k0_x=2*pi/(PixSize_Sample*ZeroPadding_Real)*u0_x;
k0_y=2*pi/(PixSize_Sample*ZeroPadding_Real)*u0_y;
k0_z=sqrt ( (n_m*k0) ^2 - k0_x.^2 - k0_y.^2);
kPixSize_Sample=2*pi/(PixSize_Sample*ZeroPadding_Real);

%% k-space Mapping
Frame_range=[65 512];                                   % select frame range for reconstruction
Rytov_Tomo=zeros(ZeroPadding_Fourier3D,ZeroPadding_Fourier3D,ZeroPadding_Fourier3D,'single');
Count=zeros(ZeroPadding_Fourier3D,ZeroPadding_Fourier3D,
ZeroPadding_Fourier3D,'single');                        % to count the number of overlapped information.

for kk=Frame_range(1):Frame_range(2)
    Rytov_2Dimage=log (squeeze (EField(kk,:,:)) );      %% set Rytov field
    padVal=(ySize*mean(Rytov_2Dimage(1,:)) + ySize*mean(Rytov_2Dimage(end,:)) + xSize*mean(Rytov_2Dimage(:,1)) +
    xSize*mean(Rytov_2Dimage(:,end)))/(2*(xSize+ySize)−4);
    Rytov_2Dimage=padarray (Rytov_2Dimage, round([(ZeroPadding_Real-xSize)
    (ZeroPadding_Real-ySize)]./2), padVal);             %zero-padding at the sample plane
    Rytov_2DFourier=fftshift (fft2 (Rytov_2Dimage))/ZeroPadding_Real;
    Rytov_2DFourier=circshift (Rytov_2DFourier, round([u0_x(kk) u0_y(kk)]));

    %% mapping to Ewald's sphere with a radius of n_m*k0
    [ky kx]=meshgrid ( (kPixSize_Sample* (1:ZeroPadding_Real) -ZeroPadding_Real/2). *[1,1]);
    kz=real (sqrt ((n_m*k0)^2 - kx.^2 - ky.^2));
    Ewald=1i.*kz.*Rytov_2DFourier/pi;                   % mapping Rytov field to Ewald sphere

    %% Select Rytov field for real k vectors
    [xtemp, ytemp]=find (kz>0);
    Xrange=min(xtemp): max(xtemp); Yrange=min(ytemp): max(ytemp);
    Ewald=Ewald(Xrange,Yrange);

    Kx=kx - k0_x(kk); Kx=Kx(Xrange,Yrange);
    Ky=ky - k0_y(kk); Ky=Ky(Xrange,Yrange);
    Kz=kz - k0_z(kk); Kz=Kz(Xrange,Yrange);

    %% Applying to 3D Rytov space
    Kx=round (Kx/kPixSize_Sample+ZeroPadding_Fourier3D/2);
    Ky=round (Ky/kPixSize_Sample+ZeroPadding_Fourier3D/2);
    Kz=round (Kz/kPixSize_Sample+ZeroPadding_Fourier3D/2);

    ZeroPadding_Real3=length(Kx);
    KZeroPadding_Real=(Kz-1)*ZeroPadding_Fourier3D^2+(Ky-1)*ZeroPadding_Fourier3D+Kx;
    KZeroPadding_Real=PixSize_Samplehape
    (KZeroPadding_Real, 1, ZeroPadding_Real3^2);        % make indexing column vector

    temp=PixSize_Samplehape (Rytov_Tomo (KZeroPadding_Real), ZeroPadding_Real3, ZeroPadding_Real3);
    Rytov_Tomo (KZeroPadding_Real)=temp+Ewald;
    Count (KZeroPadding_Real)=Count (KZeroPadding_Real)+1; % count mapped 3-D Fourier space coordinates

end

Rytov_Tomo (Count>0)=Rytov_Tomo (Count>0)./Count (Count>0); % average for overlapped points
ReconImg=ifftn (ifftshift (Rytov_Tomo)). *
(ZeroPadding_Fourier3D^(3/2));                          % transform to real space
n=n_m*sqrt (1-ReconImg.* (lambda/(2*pi*n_m)) ^2);       % convert to actual refractive index

% Iterative algorithm for optical diffraction tomography
% Programmed by Kyoohyun Kim, (Biomedical Optics Lab, KAIST) 2012-8-9
% for further information, please refer to http://bmokaist.wordpress.com

Rytov_Tomo_index=(abs(Rytov_Tomo)==0);                  % locate k position for missing cone
Iter=100; %total number of iteration
```

```
for mm=1:Iter
    constn=real(n)<n_m;                                          % criterion: nonnegative refractive index difference
    n(constn)=n_m+1i*angle(n(constn));
    F=-(2*pi*n_m/lambda)^2.*(n.^2/n_m^2-1);
    temp=fftshift (fftn (F) )/(ZeroPadding_Fourier3D^ (3/2) );   % new 3D Fourier field
    Rytov_Tomo_new=temp.*Rytov_Tomo_index+Rytov_Tomo;            % replace previously measured field Rytov_Tomo)
    F=ifftn (ifftshift (Rytov_Tomo_new) ) * (ZeroPadding_Fourier3D^ (3/2));
    n=n_m*sqrt (1 - F.* (lambda/(n_m*2*pi) ) ^2);
end
```

Acknowledgments

The authors wish to acknowledge Professor Subra Suresh (MIT and NSF) for helpful discussions. This work was funded by KAIST, the Korean Ministry of Education, Science and Technology (MEST) Grant No. 2009-0087691 (BRL), National Research Foundation (NRF-2012R1A1A1009082, NRF-2012K1A31A1A09055128, and NRF-M3C1A1-048860). YongKeun Park acknowledges support from TJ ChungAm Foundation. Kyoohyun Kim is supported by Global Ph.D. Fellowship from National Research Foundation of Korea. Monica Diez-Silva and Ming Dao acknowledge support from National Institutes of Health (R01HL094270) and the Singapore-MIT Alliance for Research and Technology (SMART) Center. Ramachandra R. Dasari acknowledges support from National Institutes of Health (9P41-EB015871-26A1), the National Science Foundation (DBI-0754339).

References

1. World Health Organization, "World Malaria Report 2012," pp. 53–62, World Health Organization, Geneva (2012).
2. L. Bannister et al., "A brief illustrated guide to the ultrastructure of Plasmodium falciparum asexual blood stages," *Parasitol. Today* **16**(10), 427–433 (2000).
3. F. Frischknecht, "Imaging parasites at different scales," *Cell Host Microbe* **8**(1), 16–19 (2010).
4. E. Hanssen et al., "Soft X-ray microscopy analysis of cell volume and hemoglobin content in erythrocytes infected with asexual and sexual stages of Plasmodium falciparum," *J. Struct. Biol.* **177**(2), 224–232 (2012).
5. C. Magowan et al., "Intracellular structures of normal and aberrant Plasmodium falciparum malaria parasites imaged by soft x-ray microscopy," *Proc. Natl. Acad. Sci. U. S. A.* **94**(12), 6222–6227 (1997).
6. S. Cho et al., "Optical imaging techniques for the study of malaria," *Trends Biotechnol.* **30**(2), 71–79 (2012).
7. B. Gligorijevic et al., "Stage independent chloroquine resistance and chloroquine toxicity revealed via spinning disk confocal microscopy," *Mol. Biochem. Parasitol.* **159**(1), 7–23 (2008).
8. Y.-K. Park et al., "Refractive index maps and membrane dynamics of human red blood cells parasitized by Plasmodium falciparum," *Proc. Natl. Acad. Sci. U. S. A.* **105**(37), 13730–13735 (2008).
9. R. Chandramohanadas et al., "Biophysics of malarial parasite exit from infected erythrocytes," *PLoS ONE* **6**(6), e20869 (2011).
10. K.-R. Lee et al., "Quantitative phase imaging techniques for the study of cell pathophysiology: from principles to applications," *Sensors* **13**(4), 4170–4191 (2013).
11. G. Popescu et al., "Diffraction phase microscopy for quantifying cell structure and dynamics," *Opt. Lett.* **31**(6), 775–777 (2006).
12. T. Ikeda et al., "Hilbert phase microscopy for investigating fast dynamics in transparent systems," *Opt. Lett.* **30**(10), 1165–1168 (2005)
13. Y. K. Park et al., "Diffraction phase and fluorescence microscopy," *Opt. Express* **14**(18), 8263–8268 (2006).
14. Y.-K. Park et al., "Speckle-field digital holographic microscopy," *Opt. Express* **17**(15), 12285–12292 (2009).
15. Y. Park et al., "Measurement of red blood cell mechanics during morphological changes," *Proc. Natl. Acad. Sci. U. S. A.* **107**(15), 6731–6736 (2010)
16. Y. K. Park et al., "Metabolic remodeling of the human red blood cell membrane," *Proc. Natl. Acad. Sci.* **107**(4), 1289–1294 (2010).
17. Y. K. Park et al., "Measurement of the nonlinear elasticity of red blood cell membranes," *Phys. Rev. E* **83**(5), 051925 (2011).
18. G. Popescu et al., "Optical imaging of cell mass and growth dynamics," *Am. J. Physiol. Cell Physiol.* **295**(2), C538–C544 (2008).
19. M. Mir et al., "Optical measurement of cycle-dependent cell growth," *Proc. Natl. Acad. Sci. U. S. A.* **108**(32), 13124–13129 (2011).
20. Y. Park et al., "Spectroscopic phase microscopy for quantifying hemoglobin concentrations in intact red blood cells," *Opt. Lett.* **34**(23), 3668–3670 (2009).
21. Y. Jang, J. Jang, and Y. K. Park, "Dynamic spectroscopic phase microscopy for quantifying hemoglobin concentration and dynamic membrane fluctuation in red blood cells," *Opt. Express* **20**(9), 9673–9681 (2012).
22. G. G. Levin et al., "Three-dimensional limited-angle microtomography of blood cells: experimental results," *Proc. SPIE* **3261**, 159–164 (1998).
23. V. Lauer, "New approach to optical diffraction tomography yielding a vector equation of diffraction tomography and a novel tomographic microscope," *J. Microsc.* **205**(2), 165–176 (2002).
24. B. Simon et al., "Tomographic diffractive microscopy of transparent samples," *Eur. Phys. J. Appl. Phys.* **44**(1), 29–35 (2008).
25. S. O. Isikman et al., "Lens-free optical tomographic microscope with a large imaging volume on a chip," *Proc. Natl. Acad. Sci.* **108**(18), 7296–7301 (2011).
26. F. Charrière et al., "Living specimen tomography by digital holographic microscopy: morphometry of testate amoeba," *Opt. Express* **14**(16), 7005–7013 (2006).
27. M. Fauver et al., "Three-dimensional imaging of single isolated cell nuclei using optical projection tomography," *Opt. Express* **13**(11), 4210–4223 (2005).
28. J. Izatt et al., "Optical coherence microscopy in scattering media," *Opt. Letters* **19**(8), 590–592 (1994).
29. M. Choma et al., "Spectral-domain phase microscopy," *Opt. Lett.* **30**(10), 1162–1164 (2005).
30. Z. Wang et al., "Spatial light interference tomography (SLIT)," *Opt. Express* **19**(21), 19907–19918 (2011).
31. G. Popescu, *Quantitative Phase Imaging of Cells and Tissues*, McGraw-Hill, New York (2011).
32. M. Potcoava and M. Kim, "Optical tomography for biomedical applications by digital interference holography," *Meas. Sci. Technol.* **19**(7), 074010 (2008)
33. J. Kühn et al., "Submicrometer tomography of cells by multiple-wavelength digital holographic microscopy in reflection," *Opt. Lett.* **34**(5), 653–655 (2009).
34. K. G. Phillips, S. L. Jacques, and O. J. T. McCarty, "Measurement of single cell refractive index, dry mass, volume, and density using a transillumination microscope," *Phys. Rev. Lett.* **109**(11), 118105 (2012).
35. N. T. Shaked et al., "Quantitative microscopy and nanoscopy of sickle red blood cells performed by wide field digital interferometry," *J. Biomed. Opt.* **16**(3), 030506 (2011).
36. Y. Kim et al., "Anisotropic light scattering of individual sickle red blood cells," *J. Biomed. Opt.* **17**(4), 040501 (2012).
37. H. S. Byun et al., "Optical measurement of biomechanical properties of individual erythrocytes from a sickle cell patient," *Acta Biomater.* **8**(11), 4130–4138 (2012).
38. E. Ben-Isaac et al., "Effective temperature of red-blood-cell membrane fluctuations," *Phys. Rev. Lett.* **106**(23), 238103 (2011).

39. Y. Park et al., "Light scattering of human red blood cells during metabolic remodeling of the membrane," *J. Biomed. Opt.* **16**(1), 011013 (2011).
40. W. Choi et al., "Tomographic phase microscopy," *Nat. Methods* **4**(9), 717–719 (2007).
41. A. G. Maier et al., "Malaria parasite proteins that remodel the host erythrocyte," *Nat. Rev. Microbiol.* **7**(5), 341–354 (2009).
42. E. Wolf, "Three-dimensional structure determination of semi-transparent objects from holographic data," *Opt. Commun.* **1**(4), 153–156 (1969).
43. Y. Sung et al., "Optical diffraction tomography for high resolution live cell imaging," *Opt. Express* **17**(1), 266–277 (2009).
44. A. J. Devaney, "A filtered back-propagation algorithm for diffraction tomography," *Ultrason. Imag.* **4**(4), 336–350 (1982).
45. K. C. Tam and V. Perezmendez, "Tomographical imaging with limited-angle input," *J. Opt. Soc. Am.* **71**(5), 582–592 (1981).
46. P. Goldie et al., "Biochemical characterization of Plasmodium falciparum hemozoin," *Am. J. Trop. Med. Hyg.* **43**(6), 584–596 (1990).
47. A. Devaney, "Inverse-scattering theory within the Rytov approximation," *Opt. Lett.* **6**(8), 374–376 (1981).
48. O. Haeberle et al., "Tomographic diffractive microscopy: basics, techniques and perspectives," *J. Mod. Opt.* **57**(9), 686–699 (2010).
49. M. Debailleul et al., "Holographic microscopy and diffractive microtomography of transparent samples," *Meas. Sci. Technol.* **19**(7), 074009 (2008).
50. S. S. Kou and C. J. R. Sheppard, "Image formation in holographic tomography," *Opt. Lett.* **33**(20), 2362–2364 (2008).
51. S. K. Debnath and Y. Park, "Real-time quantitative phase imaging by spatial phase shifting algorithm," *Opt. Lett.* **36**(23), 4677–4679 (2011).
52. B. P. Medoff et al., "Iterative convolution backprojection algorithms for image-reconstruction from limited data," *J. Opt. Soc. Am.* **73**(11), 1493–1500 (1983).
53. G. Pasvol et al., "Separation of viable schizont-infected red cells of Plasmodium falciparum from human blood," *Ann. Trop. Med. Parasitol.* **72**(1), 87–88 (1978).
54. C. Lambros and J. P. Vanderberg, "Synchronization of Plasmodium falciparum erythrocytic stages in culture," *J. Parasitol.* **65**(3), 418–420 (1979).
55. R. Barer, "Refractometry and interferometry of living cells," *J. Opt. Soc. Am.* **47**(6), 545–556 (1957).
56. O. Zhernovaya et al., "The refractive index of human hemoglobin in the visible range," *Phys. Med. Biol.* **56**(13), 4013–4021 (2011).
57. M. A. Zanner et al., "Water and urea transport in human erythrocytes infected with the malaria parasite Plasmodium falciparum," *Mol. Biochem. Parasitol.* **40**(2), 269–278 (1990).
58. J. L. Elliott, K. J. Saliba, and K. Kirk, "Transport of lactate and pyruvate in the intraerythrocytic malaria parasite, Plasmodium falciparum," *Biochem. J.* **355**(Pt 3), 733–739 (2001).
59. D. A. Elliott et al., "Four distinct pathways of hemoglobin uptake in the malaria parasite Plasmodium falciparum," *Proc. Natl. Acad. Sci.* **105**(7), 2463–2468 (2008).
60. A. Esposito et al., "Quantitative imaging of human red blood cells infected with Plasmodium falciparum," *Biophys. J.* **99**(3), 953–960 (2010).
61. J. M. A. Mauritz et al., "The homeostasis of Plasmodium falciparum-infected red blood cells," *PLoS Comput. Biol.* **5**(4), e1000339 (2009).
62. L. J. Bruce-Chwatt, *Essential Malariology*, William Heinemann Medical Books Ltd., London (1980).
63. B. Gligorijevic et al., "Spinning disk confocal microscopy of live, intraerythrocytic malarial parasites. 1. Quantification of hemozoin development for drug sensitive versus resistant malaria," *Biochemistry* **45**(41), 12400–12410 (2006).
64. G. S. Noland, N. Briones, and D. J. Sullivan, "The shape and size of hemozoin crystals distinguishes diverse *Plasmodium* species," *Mol. Biochem. Parasitol.* **130**(2), 91–99 (2003).
65. A. U. Orjih and C. D. Fitch, "Hemozoin production by plasmodium-falciparum—variation with strain and exposure to chloroquine," *Biochim. Biophys. Acta* **1157**(2), 270–274 (1993).
66. R. K. Saha, S. Karmakar, and M. Roy, "Computational investigation on the photoacoustics of malaria infected red blood cells," *PLoS One* **7**(12), e51774 (2012).
67. Y. M. Serebrennikova et al., "Quantitative analysis of morphological alterations in Plasmodium falciparum infected red blood cells through theoretical interpretation of spectral measurements," *J. Theor. Biol.* **265**(4), 493–500 (2010).
68. M. Diez-Silva et al., "Pf155/RESA protein influences the dynamic microcirculatory behavior of ring-stage *Plasmodium falciparum* infected red blood cells," *Sci. Rep.* **2**, 614 (2012).